

YAW-ROLL COUPLED OSCILLATIONS OF A SLENDER DELTA WING

Except where reference is made to the work of others, the work described in this thesis is my own or was done in collaboration with my advisory committee. This thesis does not include proprietary or classified information.

John C. Worley

Certificate of Approval:

Gilbert Crouse Jr.
Associate Professor
Aerospace Engineering

Anwar Ahmed, Chair
Associate Professor
Aerospace Engineering

Brian Thurow
Assistant Professor
Aerospace Engineering

Joe F. Pittman
Interim Dean
Graduate School

YAW-ROLL COUPLED OSCILLATIONS OF A SLENDER DELTA WING

John C. Worley

A Thesis

Submitted to

the Graduate Faculty of

Auburn University

in Partial Fulfillment of the

Requirements for the

Degree of

Master of Science

Auburn, Alabama

August 9, 2008

YAW-ROLL COUPLED OSCILLATIONS OF A SLENDER DELTA WING

John C. Worley

Permission is granted to Auburn University to make copies of this thesis at its discretion, upon the request of individuals or institutions and at their expense. The author reserves all publication rights.

Signature of Author

Date of Graduation

VITA

John Worley, son of John Allen and Susan (Cantrell) Worley, was born on April 23, 1984, in Easley, South Carolina. He graduated from D. W. Daniel High School in 2002 before entering Auburn University in the fall. In 2006, he graduated magna cum laude with a Bachelors of Aerospace Engineering. After working as a Wind Tunnel Technician in Auburn University's Aerospace Engineering department, he entered Graduate School at Auburn University in August 2006.

THESIS ABSTRACT

YAW-ROLL COUPLED OSCILLATIONS OF A SLENDER DELTA WING

John C. Worley

Master of Science, August 9, 2008
(B.S., Auburn University, 2006)

52 Typed Pages

Directed by Anwar Ahmed

The delta wing has been a highly studied aerial platform, from counter rotating vortices to a rolling ‘wing rock’ motion. The research done at Auburn University is an extension of those studies. This research studies not only the inherent roll motion of the delta wing but also the yaw motion that is coupled with that rolling motion. Using a specially designed model, a wind tunnel, and a dynamic vortex laboratory, the aerodynamics of a slender delta wing could be analyzed. The delta wing’s motion could be tracked using an accelerometer and optical encoder and the shedding vortices could be seen through various flow visualization techniques. The time histories and time averaged angle sweep data were also collected using a force and moment balance. This model also allowed for the ability to study one type of motion at a time, which allowed for comparison with previous purely rolling studies. Below are the results of both the roll and yaw motion on the slender delta wing as well as the coupled effect of the two.

ACKNOWLEDGMENTS

The author would like to thank Dr. Anwar Ahmed for providing him with this opportunity, guidance, and support throughout this work. The author would also like to thank the committee for this opportunity given to him, Mr. Bryan Recktenwald for his assistance, Mr. Andy Weldon for making all the experimental setups that made this work possible, and the Aerospace Engineering Department of Auburn University for the opportunity and financial support. The author would like to address most of his thanks to his parents for their unlimited support.

Style manual or journal used Journal of Approximation Theory (together with the style known as “aums”). Bibliography follows van Leunen’s *A Handbook for Scholars*.

Computer software used The document preparation package T_EX (specifically L^AT_EX) together with the departmental style-file aums.sty. All graphs were made using Tecplot.

TABLE OF CONTENTS

LIST OF FIGURES	ix
LIST OF TABLES	xi
1 INTRODUCTION	1
1.1 Background	1
1.2 Research Objectives	8
2 EXPERIMENTAL SETUP	9
2.1 Model Description	9
2.2 Model Geometry	11
2.2.1 Wind Tunnel Model	11
2.2.2 Water Tunnel Model	13
2.3 Test Facility Setup	14
2.3.1 Wind Tunnel	14
2.3.2 Water Tunnel	15
2.4 Data Acquisition	16
3 RESULTS AND DISCUSSION	19
4 CONCLUSIONS	34
BIBLIOGRAPHY	36
APPENDICES	38
Appendix A: Additional Plots	39

LIST OF FIGURES

1.1	Different delta wing planforms: a.) Slender[1] b.) Non-slender[2]. . . .	2
1.2	Detailed flow schematic over a delta wing[4].	3
1.3	Theoretical (potential flow) and experimental lift coefficient curves for a delta wing in subsonic flow[7].	4
1.4	Delta wing experiencing both spiral (top) and bubble (bottom) breakdown[11].	5
1.5	Negative pressure distributions over a delta wing after ‘bursting’ has occurred: a.)Upper surface b.)Rear surface.	7
1.6	Diagram of lift and weight vectors pre- and post- ‘bursting.’	7
2.1	Planform views of the delta wing model.	10
2.2	Bearing locations on the model setup.	10
2.3	Close up of wind tunnel model.	12
2.4	Close up of the acrylic plates used to lock the yaw motion.	12
2.5	Close up of water tunnel model.	13
2.6	Wind tunnel experimental setup.	16
2.7	Water tunnel experimental setup.	17
3.1	Variation in lift coefficient versus time.	20
3.2	Variation in lift coefficient and roll angle for the Roll Free case. . . .	21
3.3	LIF flow visualization of the Roll Free case (left to right from top). . .	21
3.4	Variation in lift coefficient and roll angle for the Yaw Free case. . . .	22

3.5	Depiction of a yawing delta wing: (a) Pre ‘burst’ (b) At ‘burst’ (c) Post ‘burst.’	23
3.6	LIF flow visualization of the Yaw Free case (left to right from top).	24
3.7	Variation in lift coefficient and roll angle for the All Free case.	25
3.8	Roll angle versus roll rate for the Roll Free case.	25
3.9	Roll angle versus roll rate for the All Free case.	26
3.10	LIF flow visualization of the All Free case (left to right from top).	26
3.11	LIF flow visualization of the All Free case (left to right from top).	27
3.12	Variation in pitching moment coefficient versus time.	28
3.13	Variation in rolling moment coefficient versus time.	29
3.14	Variation in yawing moment coefficient versus time.	30
3.15	Lift coefficient versus α	31
3.16	Rolling moment coefficient versus α	31
3.17	Yawing moment coefficient versus α	32
3.18	Accelerations and roll angle for the Roll Free case.	32
A.1	Drag force coefficient versus time.	39
A.2	Side force coefficient versus time.	40
A.3	Side force coefficient versus α	40
A.4	Lift coefficient versus drag coefficient.	41

LIST OF TABLES

2.1	Pyramidal balance reduction matrix.	15
2.2	Instrumentation samples and sampling rates.	18

CHAPTER 1
INTRODUCTION

1.1 Background

Delta wing planforms and the aerodynamics surrounding them have been a subject of investigation for the past several decades; however, a full picture of the flow and its effects on the aerodynamics of the wing has not yet emerged. Previous studies must therefore be improved upon in order to fully understand the flow over a delta wing.

Delta wing planforms can be categorized as either slender or non-slender. The distinguishing factor between the two is the sweep angle, Λ . This sweep angle is measured between a line perpendicular to the center line that is attached to the nose of the wing and the leading edge of the wing. As long as the sweep angle is less than $\Lambda = 55^\circ$ the delta wing is considered to be non-slender, whereas a delta wing with an angle larger than $\Lambda = 55^\circ$ is considered to be slender. Figure 1.1 shows aircraft with slender and non-slender delta wing planforms. Both non-slender and slender delta wings have been utilized on various aircraft; however, slender delta wings, with a leading edge sweep angle greater than the Mach angle, have been more attractive due to their good performance in supercritical flow regimes. For a leading edge sweep angle greater than the Mach angle, the shockwave is only attached to the nose of the wing, yielding high subsonic flow traveling over the wing. Thus a slender delta wing in supersonic flow experiences subsonic flow on the wing and has the same performance characteristics as a slender delta wing that is experiencing a purely

subsonic flow. However, tests have shown that slender delta wings have a number of stability problems at these lower speeds which generally result in an uncontrollable aircraft. In order to fully comprehend the reasons behind this stability loss, a detailed understanding of the flow over the slender delta wing is needed.



Figure 1.1: Different delta wing planforms: a.) Slender[1] b.) Non-slender[2].

The dominant flow structure over a highly swept (slender) delta wing consists of two counter rotating vortices that span the length of the wing. These counter rotating vortices are created when the shear layer of the oncoming flow separates and rolls up along the leading edge of a delta wing[3]. A detailed schematic of this flow is seen in Figure 1.2. This type of flow structure is desirable due to the fact that flow from the underside of the wing will curl up onto the upper surface feeding the vortices which in turn produce more lift[5, 6]. The amount of lift generated by the vortices can be seen in Figure 1.3 which shows the theoretical lift that a delta wing should have without the vortices and the experimental lift[7]. This vortex lift is even more desirable in modern combat aircraft and unmanned aerial vehicles (UAVs) since the increase in lift also gives an increase in maneuverability in high angle of attack regimes. However, several studies have shown that at very high angles of attack these vortices begin to

experience one of two types of degradation: spiral breakdown or bubble breakdown. A spiral breakdown occurs when the cores of one or both of the primary vortices detach from the surface of the wing but maintains its structure, forming a helix pattern downstream of the delta wing[8]. A bubble breakdown, on the other hand, occurs when the cores of one or both of the primary vortices expand and lose some of their axial flow velocity which eventually results in regions of recirculation[3, 8, 9, 10]. A depiction of both types of breakdown can be seen in Figure 1.4.

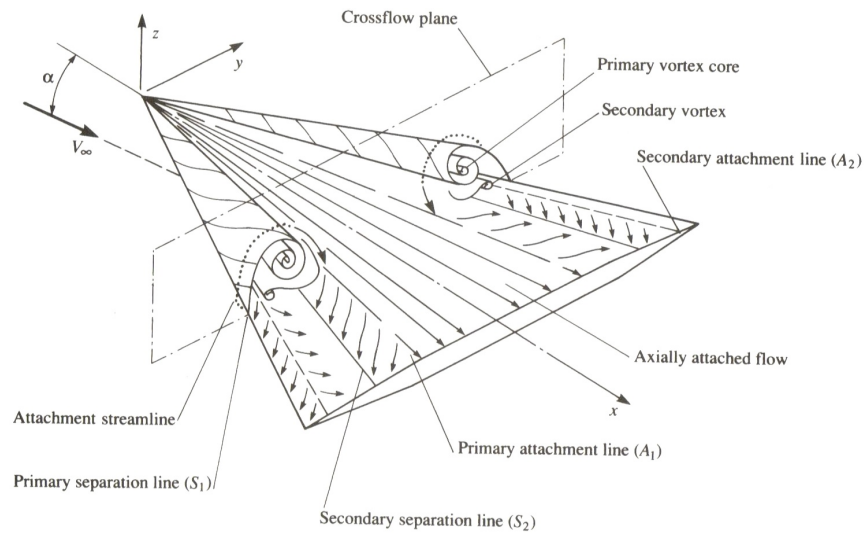


Figure 1.2: Detailed flow schematic over a delta wing[4].

So far, there is no general agreement as to what causes either of these breakdowns[12]. Although, what has been determined is that both types of breakdowns happen at some axial distance from the leading edge of the wing, usually in only one of the two primary counter rotating vortices. Since only one of the vortices has experienced this breakdown or ‘burst,’ there is an uneven lift distribution over the wing causing a rolling motion. As the delta wing rolls to one side, the vortex that has ‘burst’ begins to reform and simultaneously the other vortex ‘bursts’ causing the wing to roll back

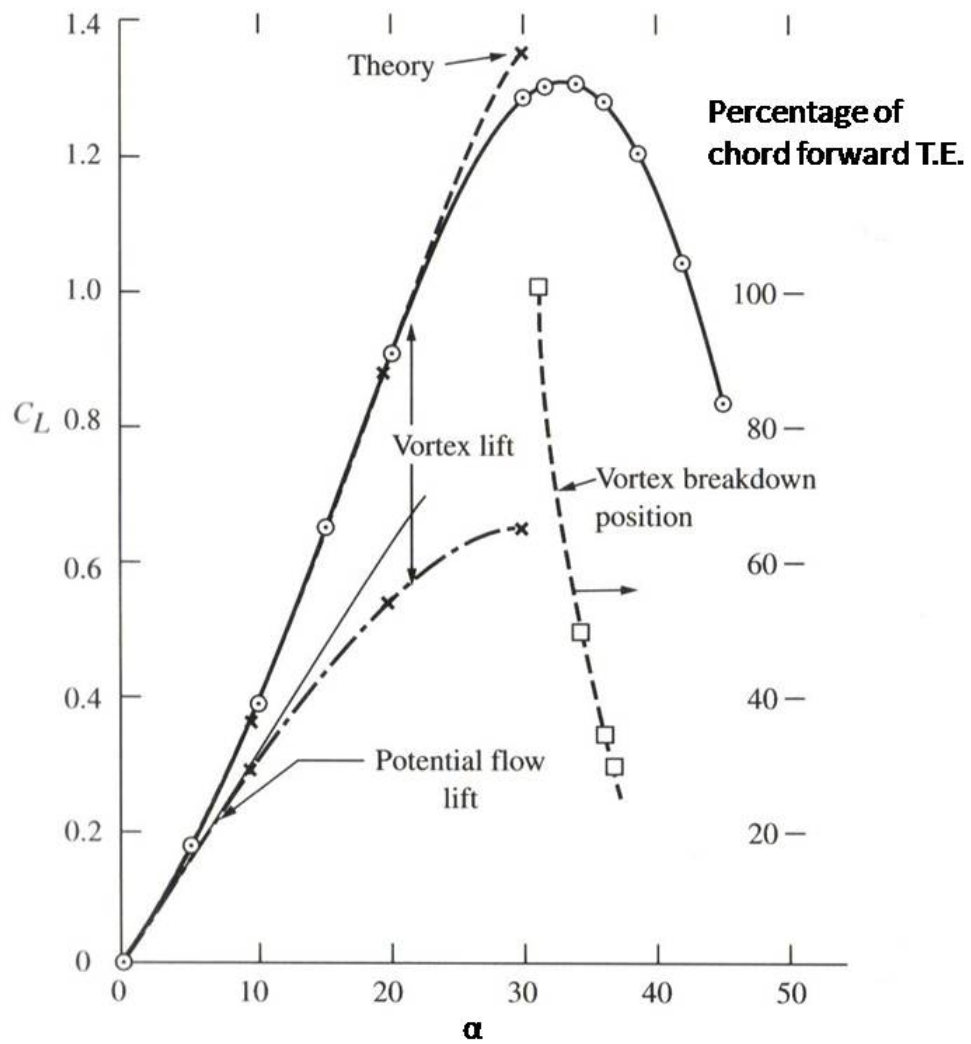
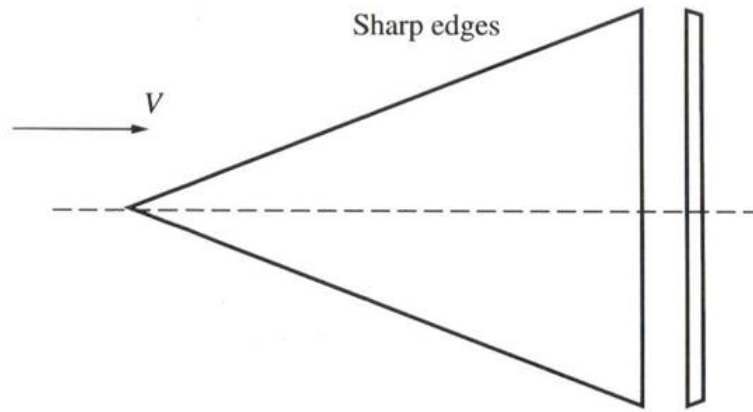


Figure 1.3: Theoretical (potential flow) and experimental lift coefficient curves for a delta wing in subsonic flow[7].

in the other direction. This rolling motion is known as a phenomenon called ‘wing rock’[3].

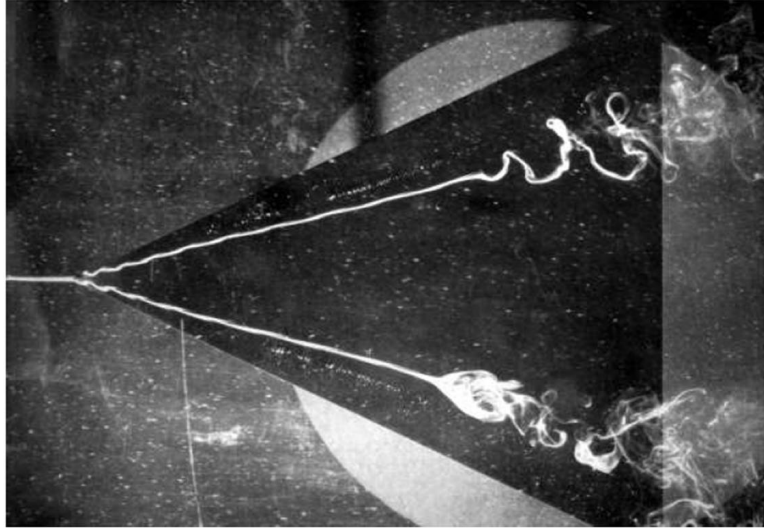


Figure 1.4: Delta wing experiencing both spiral (top) and bubble (bottom) breakdown[11].

The ‘wing rock’ phenomenon is a major focus of research. Previous investigations were conducted by mounting a slender delta wing to a wind tunnel balance either from the bottom[13] or internally from the rear[14, 15, 16]. Both types of mounting systems allowed the delta wing to undergo the self induced rolling motion that is characteristic of the ‘wing rock’ phenomenon. Data from these studies has shown a sinusoidal oscillation in the roll angle of the model[14, 15, 16]. This motion was also detected by the force balance, showing the same sinusoidal motion in the normal and side force coefficients. Time averaged studies have also been performed that illustrate the effect of the rolling motion on the lift curve[14, 17]. Results from these studies showed that the rolling motion usually increased the $C_{L_{max}}$ while the $\alpha_{C_{L_{max}}}$ remained the same. These studies also showed that there was a much larger hysteresis loop in the lift curve when the model was allowed to roll freely. Additionally, water tunnel

flow visualization results showed how the vortices formed, ‘burst,’ and interacted with each other[8, 14, 16, 17, 18].

The ‘wing rock’ phenomenon by itself does not reveal a full picture of the flow that is affecting the slender delta wing’s motion. As one of the primary vortices ‘bursts,’ the pressure distribution over the wing becomes uneven. This uneven pressure distribution causes the center of pressure to shift which results in the ‘rocking’ motion since the lift force acting at the center of pressure produces a rolling moment. This uneven pressure distribution also imparts a side force resulting in a yawing moment. The side force is produced from the tilted upper surface that forms the sharp leading edge needed to produce the counter-rotating vortices. A depiction of the negative pressure distribution over the upper surface of the wing can be seen in part (a) of Figure 1.5. This side force vector combines with the weight vector of the delta wing, resulting in a larger sideslip force that when applied at the center of pressure produces a yawing moment, as depicted in Figure 1.6. Part (b) of Figure 1.5 shows the negative pressure distribution across the rear surface, which also applies some yawing moment but to a lesser extent than that of the upper surface and weight. These unstable yawing motions coupled with the rolling motion is what causes an aircraft to go into an uncontrollable spin.

In contrast with the ‘wing rock’ motion, the yawing motion has not been explored due to the complex nature of the motion. The few studies that have been performed have only been on a delta wing with a fixed yaw, or sideslip (β), angle[14, 18, 19, 20]. The results of those investigations were compared with the data for the $\beta = 0^\circ$ cases and showed that the more the delta wing was yawed, the more detrimental the effect on the lift curve. Also, the flow visualization showed that the secondary vortex, seen in Figure 1.2, increased in size to match that of the primary vortex as the sideslip angle increased[18].

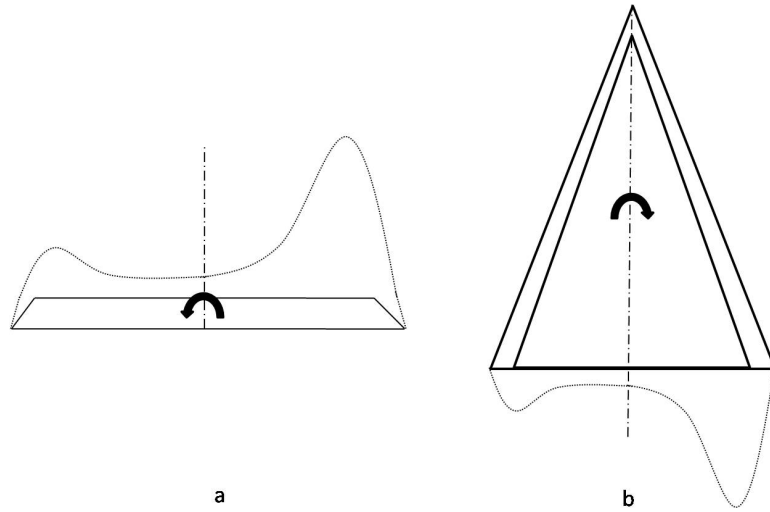


Figure 1.5: Negative pressure distributions over a delta wing after 'bursting' has occurred: a.)Upper surface b.)Rear surface.

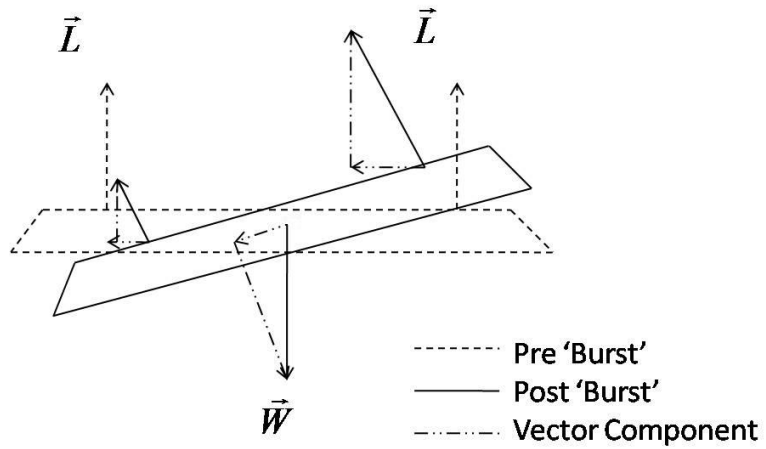


Figure 1.6: Diagram of lift and weight vectors pre- and post- 'bursting.'

1.2 Research Objectives

In order to fully understand the dynamics of a slender delta wing, every aspect must be studied in detail. Thus, the objectives of the present research are to design and manufacture two slender delta wing models capable of the full range of motions of “free flight” and to investigate the yaw-roll coupled motions using both a wind tunnel and water tunnel.

CHAPTER 2

EXPERIMENTAL SETUP

2.1 Model Description

As previously mentioned, the ‘wing rock,’ or purely rolling motion, has been studied extensively in the past. This motion was achieved in these previous studies simply by placing the slender delta wing on a shaft and then mounting that shaft on a set of ball bearings which allowed it to spin freely. However, free yawing motion has not been studied in detail due to mechanical complexities. This leads to the primary challenge of studying the yaw-roll coupled effect on a slender delta wing, which is the design and development of the research models. The only way to achieve this yawing motion without disturbing the flow is to have a delta wing with an internal bearing system. The delta wing for this experiment was then designed just thick enough to accommodate such a yaw bearing system. The yaw bearing was placed at the center of mass of the delta wing and hard mounted to the roll shaft. With both sets of bearings in place, the models had the ability to move in both the yaw and roll planes. The yaw plane is defined here as a plane that remains parallel to the upper surface of the model regardless of the roll and pitch angles. In the same fashion, the roll plane is defined as a plane that remains perpendicular to the upper surface regardless of the yaw and pitch angles. This configuration is presented in Figures 2.1 and 2.2. With simple set screws and acrylic plates, either of the motions could be locked out allowing the models to be configured to exhibit either motion independently.

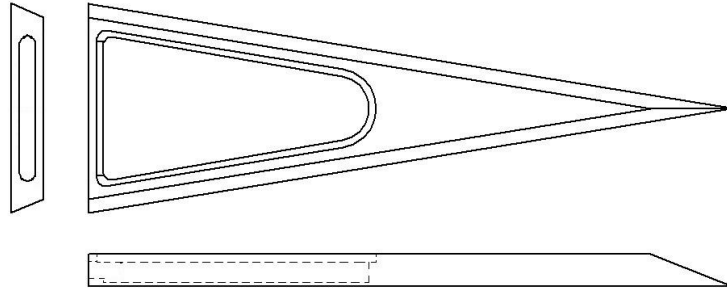


Figure 2.1: Planform views of the delta wing model.

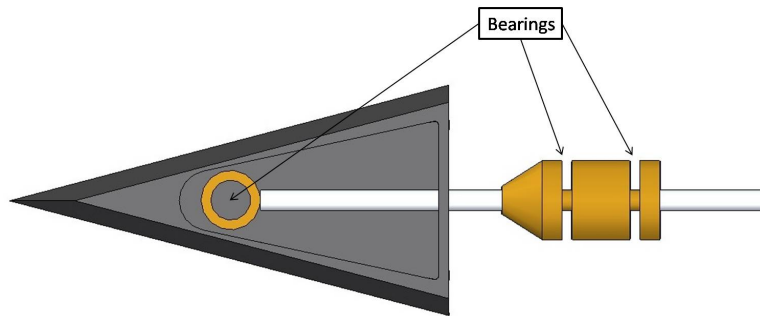


Figure 2.2: Bearing locations on the model setup.

2.2 Model Geometry

2.2.1 Wind Tunnel Model

The wind tunnel model was constructed from a solid block of aluminium. The slender criteria was met by designing the model with a leading edge sweep angle of $\Lambda = 75^\circ$. The model had a 17 in (43.18 cm) chord, a 6 in (15.24 cm) base span, and a 1 in (2.54 cm) thickness. The center of the model was hollowed out to accommodate the yaw bearing and the surrounding aluminium collar. A slot was then cut into the base to allow the 1/4 in (0.64 cm) stainless steel roll shaft to connect to the yaw bearing collar. A close up of the wind tunnel model can be seen in Figure 2.3. An acrylic plate was used to close the top of hollow chamber where the yaw bearing was placed. The acrylic plate served dual purposes: first, to close the chamber and keep the delta wing surface uniform, so as to not adversely effect the flow; second, to allow a view port to the yaw bearing, in case the roll shaft had to be disconnected. Thin acrylic plates were then made to fit on the base and around the roll shaft in order to lock the yaw motion but not impede the roll motion (Figure 2.4). The other end of the roll shaft was then slid into a brass collar that contained two stainless steel ball bearings. These bearings were placed such that the shaft would roll smoothly even with the weight of the model or a wind load being applied to one end. The distance between the base of the delta wing and the brass collar was adjustable to ensure that the flow was not affected by the mounting linkage. The brass collar also had two set screws in the rear end used to lock the roll motion in place. The ball bearings used in the brass collar and the central yaw location had 1/4 in (0.64 cm) inner diameter, a 1 in (2.54 cm) outer diameter, and a 1/4 in (0.64 cm) thickness.



Figure 2.3: Close up of wind tunnel model.



Figure 2.4: Close up of the acrylic plates used to lock the yaw motion.

2.2.2 Water Tunnel Model

The water tunnel model was designed and constructed to match the general shape and motion of the wind tunnel model. However, due to the size limitations of the water tunnel, the water tunnel model needed to be scaled down by a factor of 2.06 based on area. The same leading edge sweep angle $\Lambda = 75^\circ$ was kept while the chord and the base span were reduced to 11 in (27.94 cm) and 4.5 in (11.43 cm) respectively. The thickness of the delta wing was also reduced to $3/4$ in (1.91 cm), which in turn reduced the size of the roll shaft diameter and yaw bearing thickness to $1/8$ in (0.32 cm) each. The same type of stainless steel ball bearings were used on the roll shaft except the inner diameter was decreased to $1/8$ in (0.32 cm) to accommodate the shaft. The central yaw bearing on the other hand, had to be changed to a glass ball bearing to prevent rusting while submerged in the water. The outer surface of the model was also painted black to minimize spurious reflections of laser light during flow visualization. A close up of this model can be seen in Figure 2.5.



Figure 2.5: Close up of water tunnel model.

2.3 Test Facility Setup

2.3.1 Wind Tunnel

Once the model was constructed, a detailed study of the motions was conducted using the Auburn University's 3 ft x 4 ft (0.91 m x 1.22 m) subsonic, closed circuit, atmospheric, closed section wind tunnel. Three different instruments were used to acquire the data: a six component, force and moment, pyramidal, strain gage balance; an Endevco model 23-R triaxial piezoelectric accelerometer; and a HB6M US Digital hollow bore optical encoder. The pyramidal balance was calibrated using a series of weights that ranged from 1 lb to 30 lbs[21]. A reduction matrix was then created to determine the coupling effects between the different components of the balance. This reduction matrix was then used to calculate the loads experienced on the balance during testing. The reduction matrix that was used for this study is seen in Table 2.1. To insure that the calibration of the balance remained true, test loads were applied before any testing was performed. If the test load readings differed from the true weight by more than 1 % then the calibration process was repeated. The triaxial accelerometer was connected to its own signal conditioner which provided an output of micro-g's and had a charged response frequency of 20 Hz to 10 kHz[22]. The optical encoder was able to track the roll shaft up to 6000 RPM at a maximum sampling frequency of 10 KHz[23]. Since the output from the optical encoder was in volts, a calibration curve was applied to the signal to obtain the roll angle. The calibration curve was generated by placing a digital protractor on the roll shaft and obtaining the voltage readings from the optical encoder every 2° for a range of -60° to 60° ± 1°.

The model was connected to the pyramidal balance via a specially designed mounting system (Figure 2.6). This mounting system was designed to extend the angle of attack range of the tunnel by 10° since the standard mounting systems have

Table 2.1: Pyramidal balance reduction matrix.

Force or Moment	Normal	Pitching	Axial	Side	Rolling	Yawing
Normal	17.7596	0.5705	0.2023	0.0082	-0.0734	0.1968
Pitching	0.0738	-4.140	0.001	0.0589	-0.0216	0.0095
Axial	0.0499	-0.2768	3.7944	-0.2085	0.037	0.1518
Side	-0.2857	-0.066	0.0193	10.3528	0.6452	-0.0425
Rolling	0.0164	0.0312	-0.0137	0.0067	4.4716	-0.017
Yawing	0.0227	-0.0339	-0.0051	0.2168	-0.0154	-7.0653

an angle of attack limit of 20° and the higher angle regimes are of more interest in this study. For this study the mounting system was also articulated in such a way as to keep the model in the center of the test section so that wall boundary effects could be neglected. A shroud was then placed around the mounting system to reduce its effects on the pyramidal balance during wind loading. The triaxial accelerometer was mounted at the center span on the rear surface of the model with the x, y, and z axes oriented in the normal, span wise, and axial directions respectively. The wires to the accelerometer were then run down and through the shroud and secured so that the tension would not effect the delta wing's motion during testing. Lastly, the optical encoder was slid onto the roll shaft behind the brass sleeve. The internal bearing of the optical encoder was attached to the roll shaft via two set screws, while a bracket was attached to the outer casing and the brass sleeve of the mounting system to insure that the optical encoder's calibration stayed true.

2.3.2 Water Tunnel

Flow visualization tests were conducted in the Auburn University's 18 in x 18 in (0.46 m x 0.46 m) water tunnel. The delta wing was mounted in such a way that the angle of attack could be adjusted without submerging the roll bearings in the water. This was done so that only one glass ball bearing was needed since a metal bearing

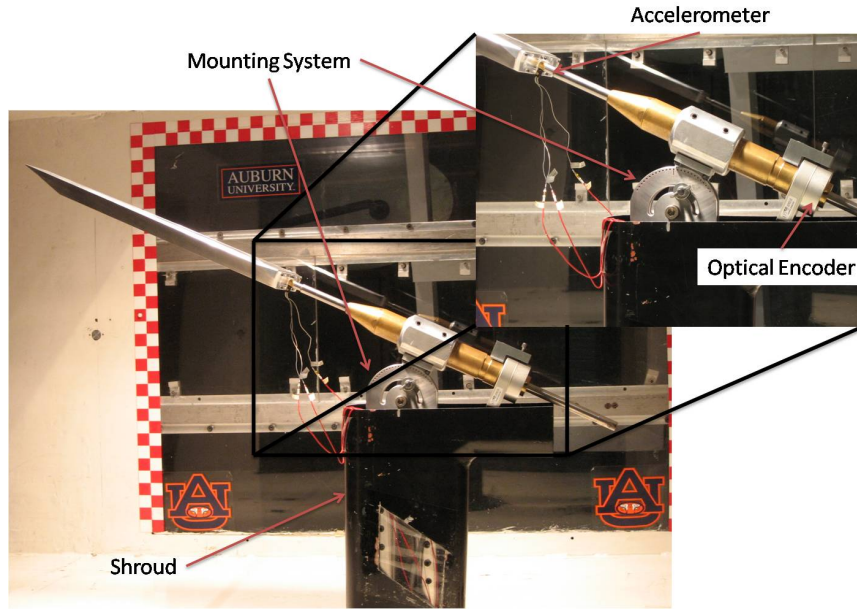


Figure 2.6: Wind tunnel experimental setup.

would rust with prolonged exposure to the water. Video data was collected using a camera at the rear of the water tunnel test section. The camera captured images of laser-induced fluorescence (LIF) of Sodium Fluorescein salt dye as it passed over the delta wing model. A 5 watt Argon Ion laser beam was passed through an OZ Optics fiber coupler to generate the laser light sheets that illuminated the Sodium Fluorescein salt dye. A diagram of this setup can be seen in Figure 2.7. The laser sheet was first placed at the mid chord and then at 1/4 chord past the trailing edge. This allowed for visualization of the vortices both during and well after breakdown.

2.4 Data Acquisition

In both the wind and water tunnels, the experiments were performed for four different cases: “none free,” “roll free,” “yaw free,” and “all free.” For the none free case, both the rear set screws on the roll shaft and the acrylic plates were screwed in

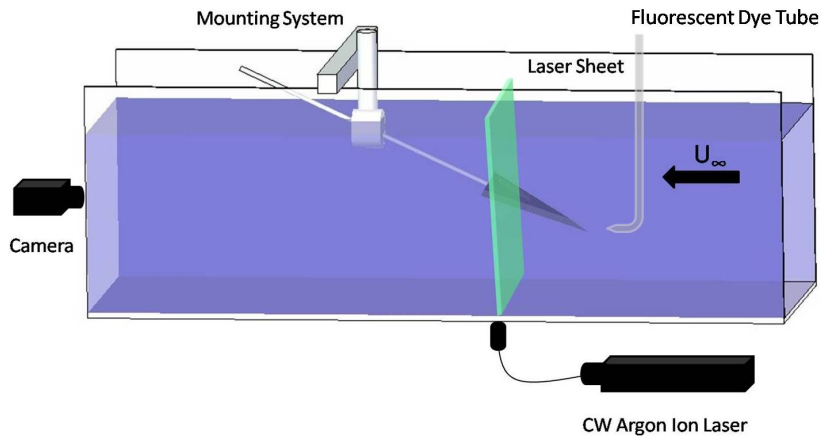


Figure 2.7: Water tunnel experimental setup.

place to lock the roll and the yaw motion respectively. This also resulted in a static baseline case to which all the other cases were compared. The roll free case had the acrylic plates in place to restrict the yaw motion, but the roll shaft was completely free to move. This allowed for the direct comparison with previously published ‘wing rock’ data. Finally the last two cases had the acrylic plates removed but one had the roll shaft set screws in place and the other did not (yaw free and all free respectively).

The wind tunnel tests were later categorized into two types: angle fixed and angle sweep. For the angle fixed tests the angle of attack (α) of the delta wing was held constant at $\alpha = 28^\circ$. This allowed for the instrumentation to acquire data for an extended amount of time (4 seconds) for time histories and mean values. The pyramidal balance data consisted of the forces and moments at each time whereas the triaxial accelerometer output was integrated twice to obtain displacements. The optical encoder was used to collect the roll angle (ϕ) at each time to correlate the forces and moments with the roll angle and to verify the triaxial accelerometer readings.

In addition, an angle sweep was also conducted whereby the delta wing model was swept through an angle of attack range of $\alpha = -3^\circ$ to $\alpha = 28^\circ$. At each angle of attack, data was acquired from the pyramidal balance for 3 seconds and then averaged to obtain the forces and moments for that angle. The triaxial accelerometer and optical encoder were not used during this set of tests.

For all of the wind tunnel testing the test section velocity was set to $110 \text{ ft/s} \pm 2 \text{ ft/s}$ (33.53 m/s), which corresponds to a Reynolds number of 9.93×10^5 based on the model's root chord. All of the data was acquired using a National Instruments 16 bit resolution analog to digital converter board. The data was then saved and processed using a Lab View virtual instrument and Tecplot. The number of samples and the sampling rates of each of the instruments used are presented in Table 2.2.

Table 2.2: Instrumentation samples and sampling rates.

	Number of Samples	Sampling Rate (Hz)
Pyramidal Balance	400	100
Triaxial Accelerometer	4000	1000
Optical Encoder	200	50

The water tunnel tests were conducted for flow visualization at the mid chord and 1/4 chord downstream of the trailing edge of the model. These tests utilized a test section velocity of 1.98 ft/s (0.61 m/s) which corresponds to a Reynolds number of 1.70×10^3 . Video images of the Sodium Fluorescein salt dye as it passed over the mid chord were recorded for each of the four cases. The laser light sheet was recorded at 250 frames per second using a JVC BR-S622DXU professional video recorder.

CHAPTER 3

RESULTS AND DISCUSSION

The wind tunnel data was plotted in Tecplot so that the different cases could be compared and conclusions about each case could be made. The water tunnel video was digitized so that screen shots could be captured and the video could be analyzed one frame at a time.

The lift was observed to have a sinusoidal characteristic when the model was free to roll. The motion started at the same level as the yaw free case (Figure 3.1) but then increased to a point and returned to the starting position. This oscillatory motion could be explained by the fact that while one of the vortices was present over one side of the wing the lift was increased and the wing was rolled to that side, but when the vortex ‘burst’ the lift decreased and the wing rolled back in the other direction. This motion can also be seen in Figure 3.2 which shows the lift force and roll angle versus time. It should be noted that the rolling motion should be symmetric yielding in an average roll angle of $\phi = 0^\circ$. The reason for the positive average angle in Figure 3.2 is possibly due to a slight weight imbalance in the model, causing the model to have a larger weight vector on one side resulting in a increased roll angle on that side.

The water tunnel flow visualization also showed self induced rolling oscillation due to the vortex ‘bursting.’ This can be seen in Figure 3.3 which shows the still images from the LIF flow visualization video. Here the self induced rolling motion can be seen by the model body rolling in a counterclockwise direction and the ‘bursting’ is seen by a lack of fluorescent dye on one side. The dye is injected into the flow via the dye tube (Figure 2.7), it then flows over the surface of the model and is

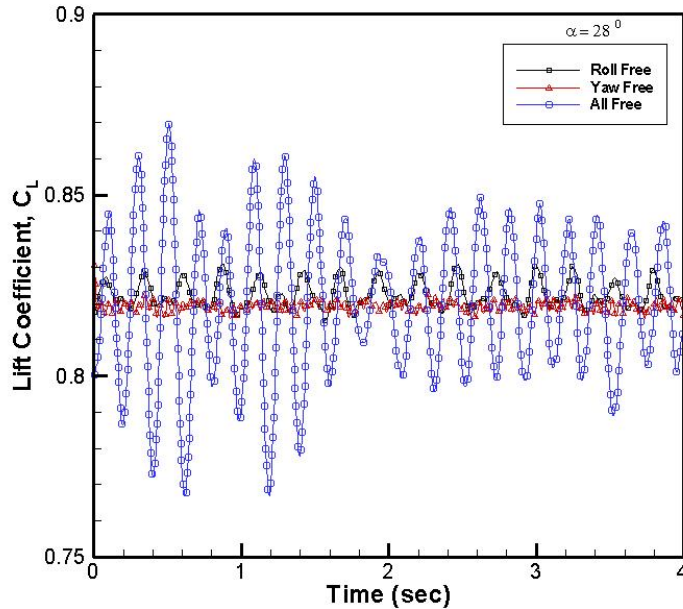


Figure 3.1: Variation in lift coefficient versus time.

drawn toward the part of the flow that has a higher velocity. Thus the lack of dye represents the ‘bursting’ phenomenon because the ‘un-burst’ vortex will have higher core velocity drawing more of the dye to that side. These results were very similar to other studies that have focused purely on the rolling delta wing (Ref [14, 15]). Both the roll angle and the lift coefficient versus time presented also matched with other studies (2 roll angle periods per second), however the amplitude was observed to be less than the present work (peaks at $25^\circ - 30^\circ$ instead of $35^\circ - 40^\circ$). This difference can be attributed to an increase in test section velocity to 110 ft/s (33.53 m/s) from 25 m/s (82.02 ft/s) [15] and 15 m/s (49.21 ft/s) [14].

The yaw free case showed very little oscillations in the lift (Figure 3.4), indicating that the sinusoidal motion was a consequence of the rolling motion. The average lift was also decreased from that of the roll free case indicating that the amount of vortex

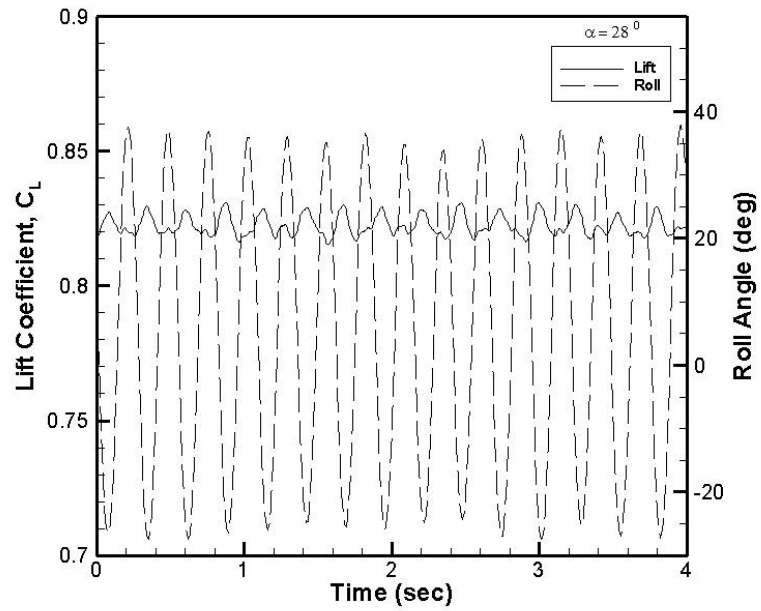


Figure 3.2: Variation in lift coefficient and roll angle for the Roll Free case.

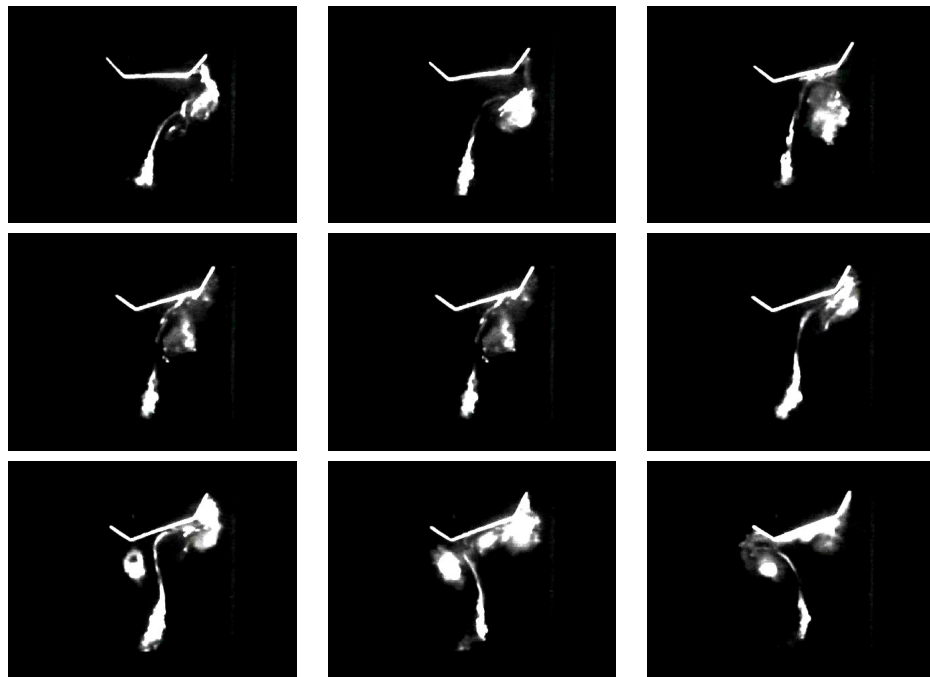


Figure 3.3: LIF flow visualization of the Roll Free case (left to right from top).

lift was less for the yaw free case than for the roll free case. A diagram of a yawing delta wing can be seen in Figure 3.5, where part (a) depicts the delta wing prior to ‘bursting’ and part (c) shows the result after ‘bursting’ where the model has slid under the vortex due to the yawing moment imposed by the uneven pressure distribution over the surface of the delta wing as discussed in Chapter 1. This process yields a portion of the delta wing without a vortex to produce lift.

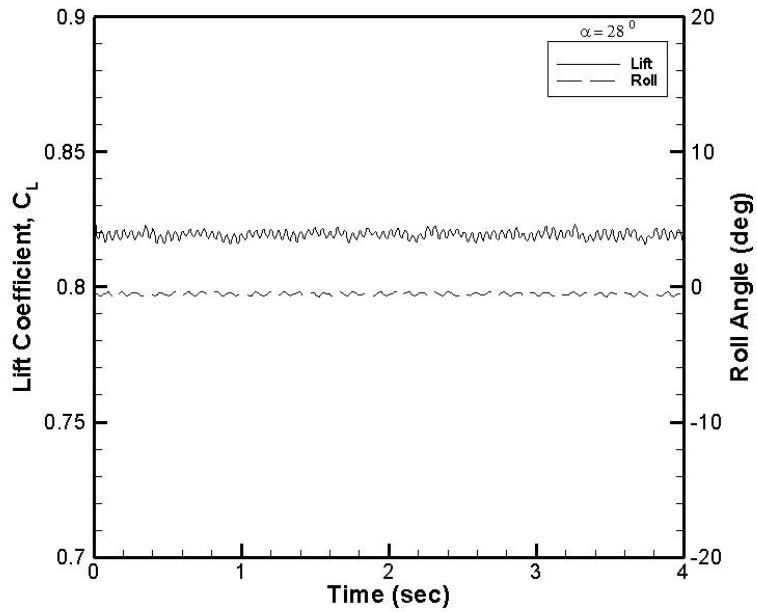


Figure 3.4: Variation in lift coefficient and roll angle for the Yaw Free case.

Flow visualization of the yaw free case showed the presence of a very unstable set of vortices. Figure 3.6 shows that the ‘un-burst’ primary vortex moved up from the surface of the model while the secondary vortex increased in size. Both vortices then yaw with the model until ‘bursting’ of both vortices has occurred. The movement of these vortices were similar to the depiction in Figure 3.5, however the flow

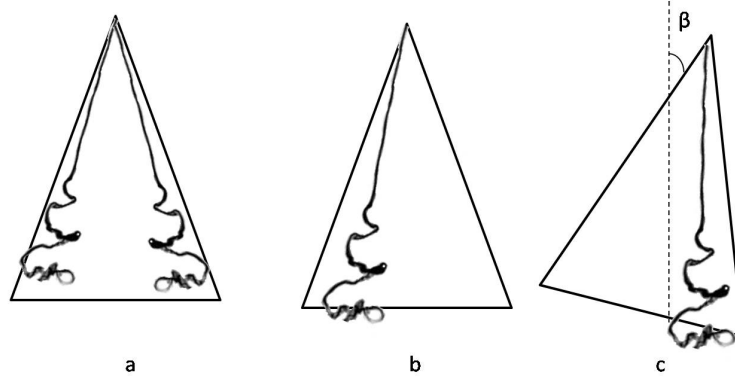


Figure 3.5: Depiction of a yawing delta wing: (a) Pre ‘burst’ (b) At ‘burst’ (c) Post ‘burst.’

visualization shows that both the model and the vortex yaw to one side before ‘bursting’ occurs in that vortex, yawing the model back in the other direction. Since the previous work on a yawing delta wing is limited there are no comparisons for the lift force vs time, however in some flow visualization studies of a statically sideslipped delta wing, the same unstable set of vortices could be seen (Ref [18, 19]).

With the combined motion (the all free case) there was a more drastic effect on the lift. Figure 3.7 shows that the all free case has a similar lift decrease and roll angle change to that of the roll free case. However, from visual observations of the model during testing, the delta wing yawed to one side while the roll angle continued to increase in the direction of the yaw until the wing began to yaw back in the other direction. This was the reason for an overlying frequency on the roll angle versus time for the all free case (Figure 3.7). This also indicated that the roll angle did not complete a full cycle until the wing had yawed back to the other direction which is further shown in Figures 3.8 and 3.9. Here Figure 3.8 shows that the rolling motion was cyclic and repetitive whereas Figure 3.9 shows that the coupled motion was cyclic but not repetitive. This indicates that the roll angle for the roll only motion

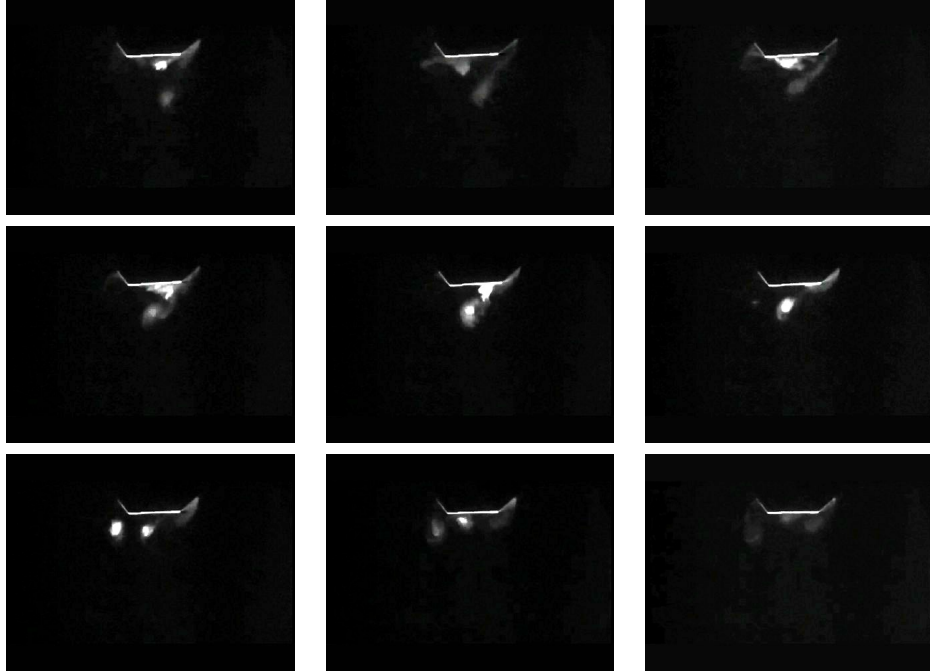


Figure 3.6: LIF flow visualization of the Yaw Free case (left to right from top).

is symmetric whereas for the coupled motion the roll angle is shifted to one side due to the yawing motion.

Figure 3.10 and Figure 3.11 show the flow visualization of the all free case. Here Figure 3.10 has an initial clockwise roll direction and a left to right yaw direction, whereas Figure 3.11 has an initial counterclockwise roll direction and a right to left yaw direction. These figures show the same unstable vortex set that the yaw free case showed but with larger vortices similar to the ones seen in the roll free case. These images also indicated that the ‘un-burst’ vortex moved to one side similar to the yaw free case, but the vortex was larger in size causing an increase in the amount of vortex lift experienced by the wing.

The same oscillatory motion can be seen in the pitching, rolling, and yawing moment plots (Figures 3.12 - 3.14). The roll free case again exhibited a sinusoidal pattern for the pitching, rolling, and yawing moments. The highest peaks occurred

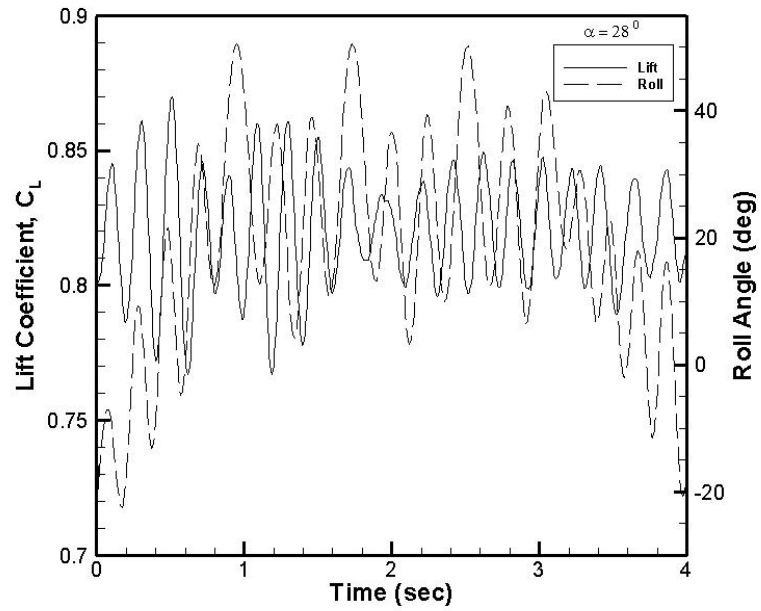


Figure 3.7: Variation in lift coefficient and roll angle for the All Free case.

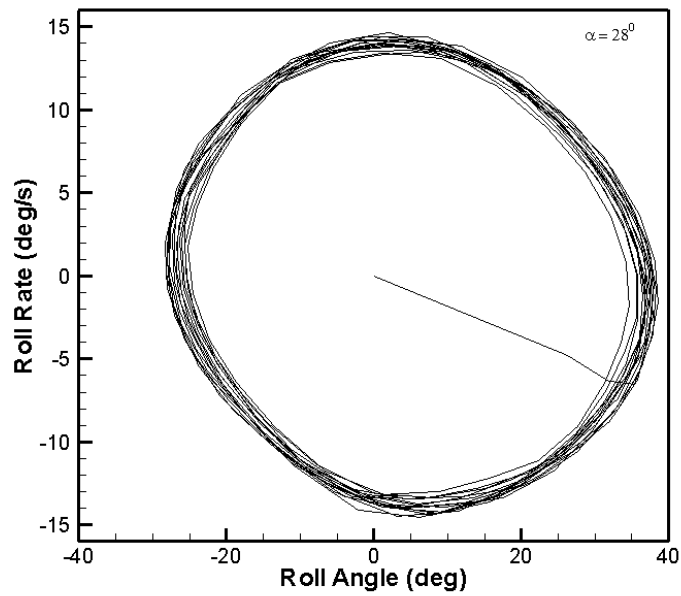


Figure 3.8: Roll angle versus roll rate for the Roll Free case.

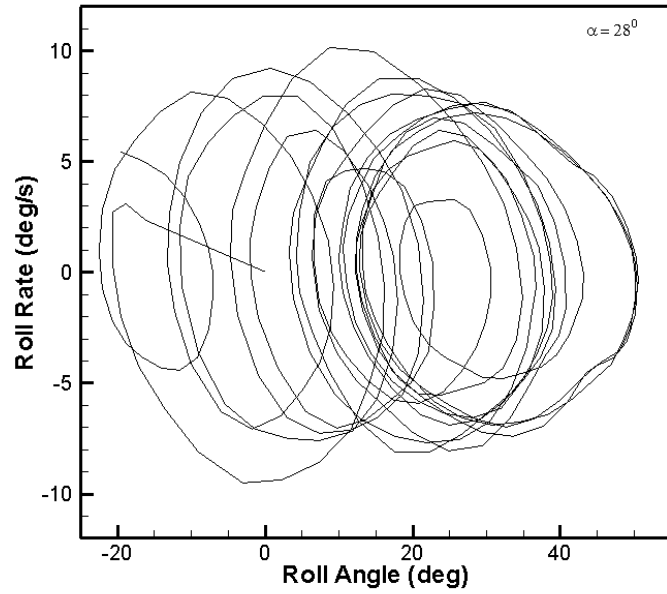


Figure 3.9: Roll angle versus roll rate for the All Free case.

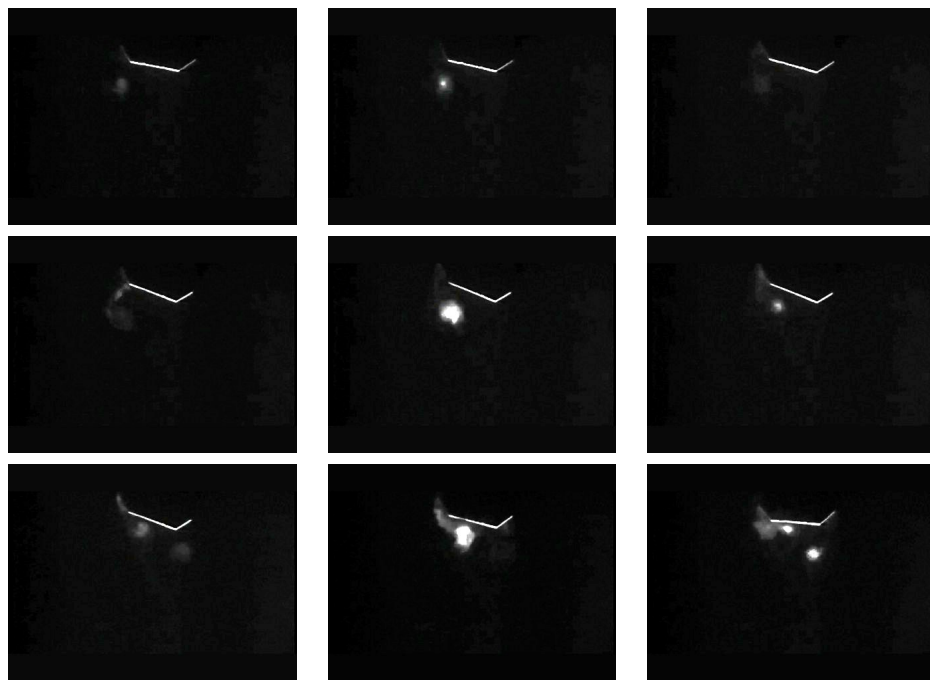


Figure 3.10: LIF flow visualization of the All Free case (left to right from top).

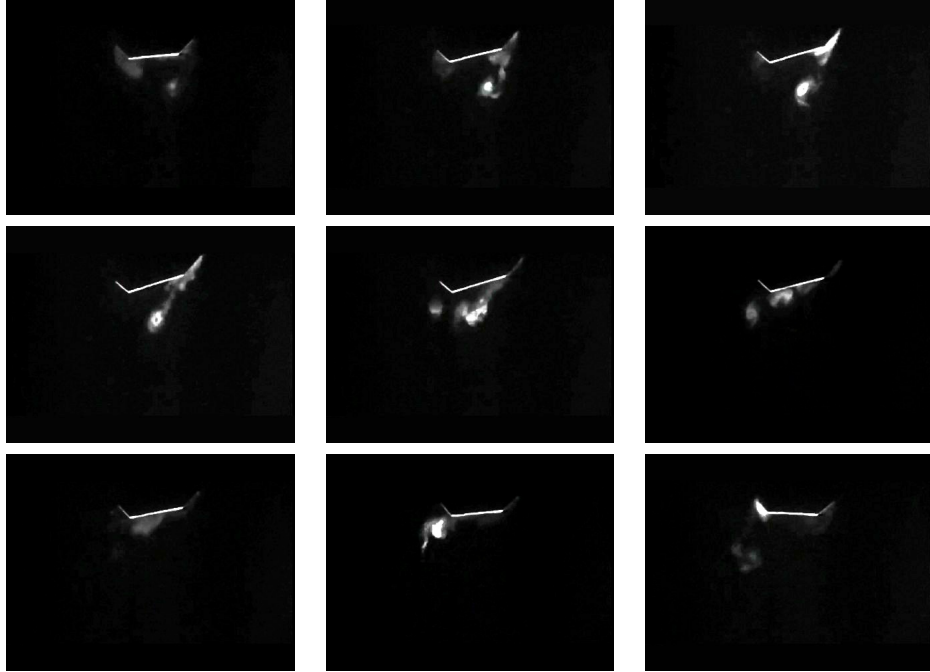


Figure 3.11: LIF flow visualization of the All Free case (left to right from top).

with the yawing moment since the lift, which was the largest force acting on the balance, was rotated to the side with the roll angle causing a twisting motion on the balance. The pitching moment was less affected since the lift, which was reduced by the maximum effect of the weight of the model, was only aligned to twist in the pitching direction when the roll angle approached zero. The yaw free case showed that all three moments remained nearly constant with the largest fluctuations coming in the yawing moment. This was again caused by a shifted lift, but not as much as seen in the roll free case. The largest fluctuations in all three moments came for the all free case. As in the lift versus time graph (Figure 3.1), the all free case showed a large non repetitive oscillation in the moment plots. The only variation was in the yawing moment (Figure 3.14) where an overlying sinusoidal oscillation was present.

The effect that all three cases had on lift coefficient for an angle sweep ($\alpha = -3^\circ$ to $\alpha = 28^\circ$) was also studied. Figure 3.15 shows that the roll free case was in line with

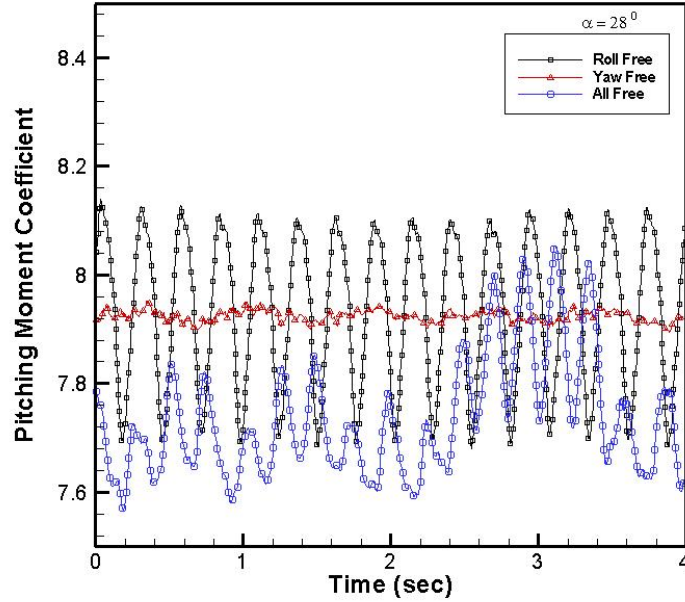


Figure 3.12: Variation in pitching moment coefficient versus time.

the none free case until the rolling motion started at $\alpha = 23^\circ$. After this transition angle the lift curve starts to decrease. The same trend is seen in the yaw free and all free cases, however the detriment to the lift curve is increased. The decrease in the lift curve is greatest for the yaw free case, meaning that the rolling motion in the all free case helps recover some of the lost lift from the yawing motion. This seems to contradict Figure 3.1 since the lift force is affected by the all free case more than the others. However, since the data taken during the angle sweep tests was averaged, the large oscillations were canceled out giving the all free case a higher overall lift when compared to the yaw free case. The large hysteresis loop observed in other works (Ref [17]) could not be observed since 28° angle of attack was not steep enough to completely stall the model.

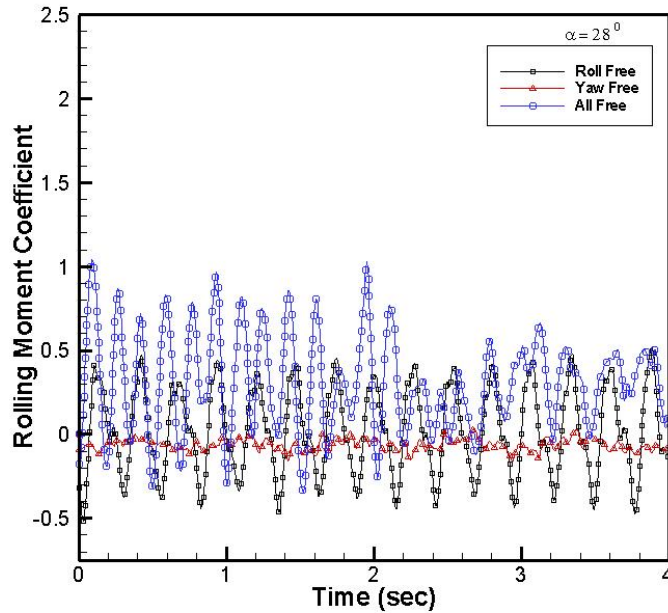


Figure 3.13: Variation in rolling moment coefficient versus time.

A similar trend could be seen with the rolling and yawing moment coefficients (Figures 3.16 and 3.17 respectively). All of the cases follow the trend of the none free static case until the transition angle of attack ($\alpha \approx 23^\circ$). Once this transition angle was reached, the moments began to decrease, with the largest decrease observed for the all free case.

A triaxial accelerometer was also used on the roll and all free cases to record the trajectory of its mounting location over time. The results of this sensor were brought into question when they were compared to the results produced by the optical encoder. Figure 3.18 shows the accelerations from the triaxial accelerometer plotted with the roll angle from the optical encoder. Since the rolling motion produces a sinusoidal roll angle versus time then the accelerations should be zero when the roll angle peaks and approach a maximum when the roll angle approaches zero. This trend

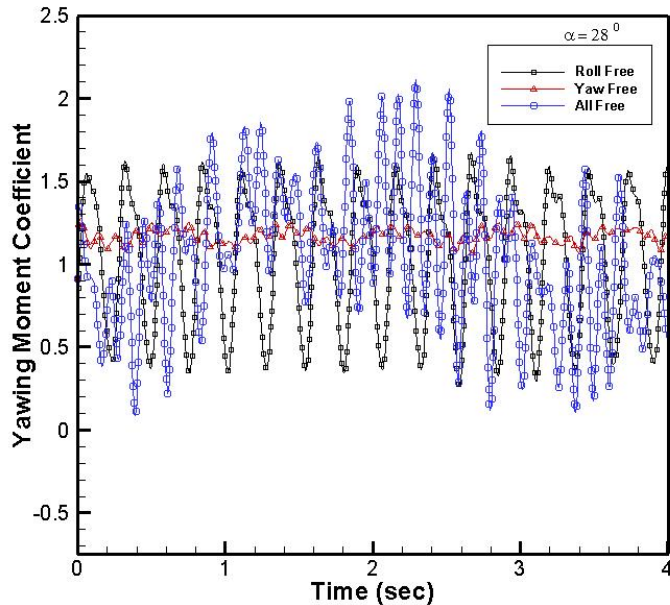


Figure 3.14: Variation in yawing moment coefficient versus time.

however is not observed in Figure 3.18. One possible reason for this difference was the proximity of the triaxial accelerometer to the roll axis causing very low accelerations on the sensor which were damped out of the signal by noise. This rendered the triaxial accelerometer unreliable and therefore the motion of the delta wing model was tracked solely by the optical encoder.

The remaining forces (drag, Figure A.1, and side force, Figure A.2-A.3) along with the drag polar (Figure A.4) have been plotted in Appendix A. These plots show similar trends to the ones seen in the lift and moment curves. The only difference arose in the side force versus time plot. This plot showed that the side force experienced the same sinusoidal oscillations that the lift did, however the phase of the curve was shifted. This indicates that when the delta wing model rolled to one side the lift force

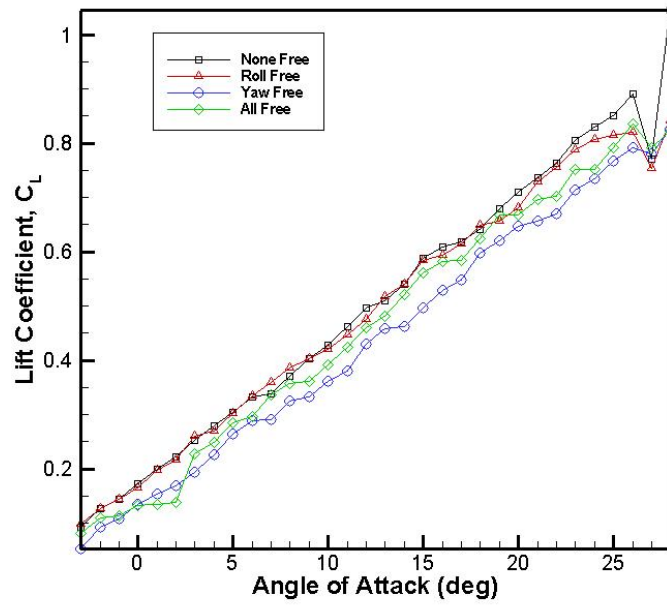


Figure 3.15: Lift coefficient versus α .

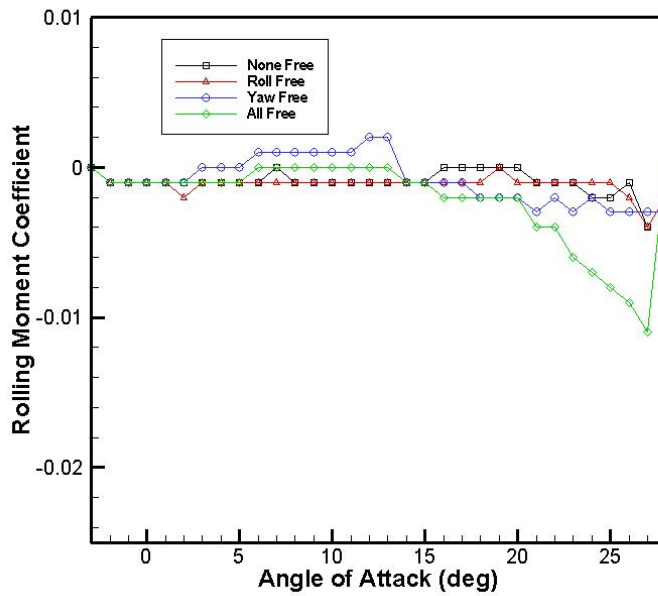


Figure 3.16: Rolling moment coefficient versus α .

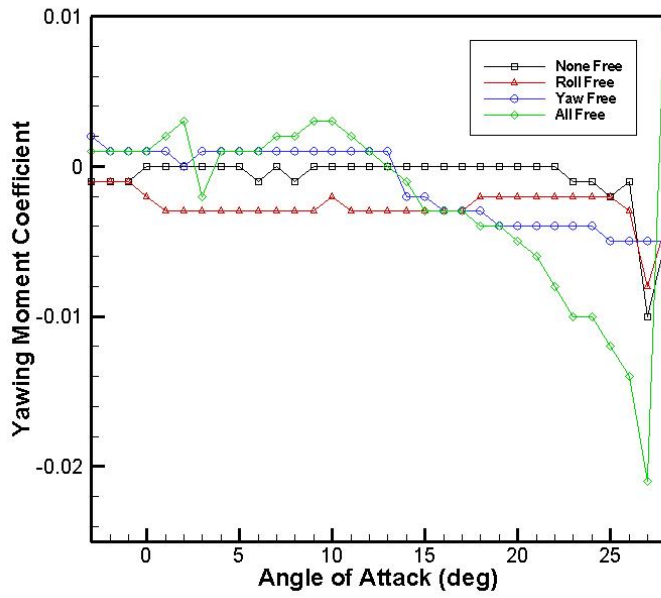


Figure 3.17: Yawing moment coefficient versus α .

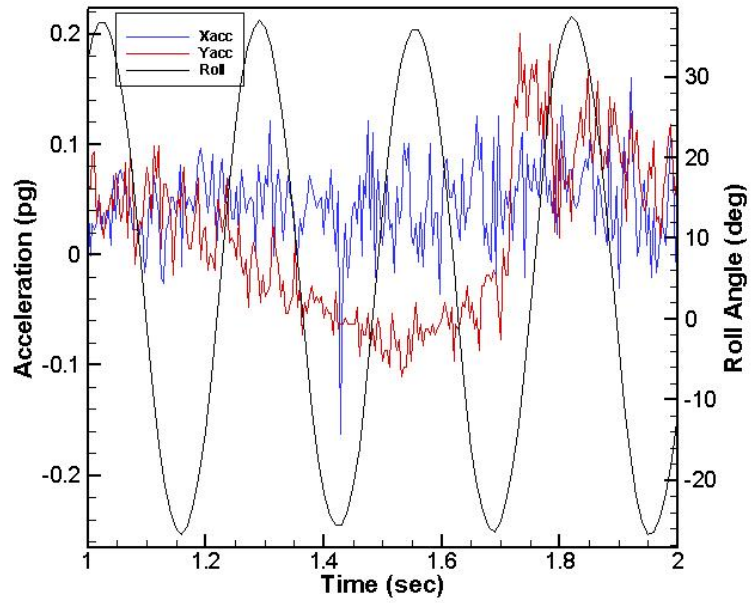


Figure 3.18: Accelerations and roll angle for the Roll Free case.

would be taken out of the normal direction and tilted to one side causing the balance to register the load on the side force component.

CHAPTER 4

CONCLUSIONS

The aerodynamics of a slender delta wing capable of two-degree of freedom motion was investigated using both a wind tunnel and water tunnel. A strong yaw-roll coupling was observed. There existed a transition angle ($\alpha \approx 23^\circ$) at which the the yaw-roll coupling began to affect the aerodynamic characteristics of the delta wing. This change was seen in the moment curves as well as the lift curve.

The findings presented here mirrored those of previous studies conducted on one-degree of freedom slender delta wings. The only differences in the results came in increased amplitudes which could be attributed to an increased test section velocity.

The yaw-roll coupling caused a sinusoidal oscillation in the moment versus time curves (Figure 3.12 - 3.14). These oscillations were similar to the oscillations seen in the roll free case, but had a larger amplitude and also had an overlying oscillation causing the entire curve to shift. The lift versus time curves exhibited similar trends with the yaw-roll coupling producing larger amplitude oscillations than that of the other cases. The only exception came from the yaw free case that produced a near constant lift line versus time. This showed that the oscillations were purely a consequence of the rolling motion. Also the yaw free case had a lower average lift indicating that it did not have the increased vortex lift that the other cases did.

The lift curve versus angle of attack showed that yaw-roll coupling decreased the amount of lift produced by the delta wing when compared to that of the none free and roll free cases. The yaw free case however, showed an even greater decrease in

lift. This further indicated that the amount of vortex lift generated by the yaw free case was less than the other cases.

The motions of the slender delta wing observed here show that the aerodynamic forces have a greater effect than the body forces. This means that the weight of the model did affect the yawing motion, however since the model was able to return to its original position and then yaw in the other direction, the weight was counteracted by the uneven pressure distribution over the surfaces of the model.

Recommendations for future work would include measuring the yaw angle in order to correlate with the roll angle and normal force time histories. Also the sweep angle could be altered to see how the yaw-roll coupling is affected. In order to reduce the contribution of the weight vector on the yawing motion, a lighter model could be designed and manufactured. Particle image velocimetry (PIV) studies could also be performed to observe the speed and strengths of the primary vortices during the motion. Addition of control surfaces could be made to the model to study their effects on the coupled motion.

BIBLIOGRAPHY

- [1] Curry, M., "Past Project - Eclipse Tow Launch Demonstration," URL: <http://www.nasa.gov/centers/dryden/history/pastprojects/Eclipse/index.html> [cited 13 March 2008].
- [2] Roberts Aerospace Manufacturing and Engineering Corporation. "Our Work - Photo Gallery," URL: <http://www.ramec.net/photoOurWork4.html> [cited 13 March 2008].
- [3] Lopez, J. M., 1990, "Axisymmetric vortex breakdown Part 1. Confined swirling flow," *Journal of Fluid Mechanics*, Vol. 221, pp. 533-552.
- [4] Anderson, J. D., Jr., *Fundamentals of Aerodynamics*, 3rd ed., McGraw-Hill, Inc., New York, NY, 2001, pp. 398-408.
- [5] Alrutz, T., and Ritten, M., "Investigation of Vortex Breakdown over a Pitching Delta Wing applying the DLR TAU-Code with Full, Automatic Grid Adaptation," 35th AIAA Fluid Dynamics, 6-9 June, Toronto, 2005, Paper No. 2005-5162.
- [6] Gursul, I., Allan, M. R., Badcock, K. J., 2005, "Opportunities for the integrated use of measurements and computations for the understanding of delta wing aerodynamics," *Aerospace Science and Technology*, Vol. 9, pp. 181-189.
- [7] Anderson, J. D., Jr., *Aircraft Performance and Design*, McGraw-Hill, Inc., New York, NY, 1999, pp. 90-104.
- [8] Huang, X. Z., and Verhaagen, N. G., "Highlights of NATO RTO Task Group AVT-080: Vortex Breakdown Over Slender Wings," 21st AIAA Applied Aerodynamics, 23-26 June, Orlando, 2003, Paper No. 2003-3939.
- [9] Gursul, I., 1994, "Unsteady Flow Phenomena over Delta Wings at High Angle of Attack," *AIAA Journal*, Vol. 32, No. 2, pp. 225-231.
- [10] Addington, G., and Jenkins, J., "Flow Visualization of a Rolling Delta Wing and Its Pertinence to the Nonlinear Indicial Response Model," 11th AIAA Applied Aerodynamics, 9-11 August, 1993, Paper No. 93-3469.

- [11] Lambourne, N. C. and Bryer, D. W., "The Bursting of Leading-Edge Vortices - Some Observations and Discussions of the Phenomenon," Reports and Memoranda 3282, Aeronautical Research Council, 1962.
- [12] Liu, Z. L., Su, C., Svoboda, J., 2006, "Variable phase control of wing rock," *Aerospace Science and Technology*, Vol. 10, pp. 27-35.
- [13] Ericsson, L. E., King, H. H. C., 1992, "Rapid Prediction of High-Alpha Unsteady Aerodynamics of Slender-Wing Aircraft," *Journal of Aircraft*, Vol. 29, No. 1, pp. 85-91.
- [14] Levin, D., Katz, J., 1984, "Dynamic Load Measurement with Delta Wings Undergoing Self-Induced Roll Oscillations," *Journal of Aircraft*, Vol. 21, No. 1, pp. 30-36.
- [15] Katz, J., Levin, D., 1986, "Self-Induced Roll Oscillations Measured on a Delta Wing/Canard Configuration," *Journal of Aircraft*, Vol. 23, No. 11, pp. 814-819.
- [16] Jun, Y. W., and Nelson, R. C., "Leading Edge Vortex Dynamics on a Delta Wing Undergoing a Wing Rock Motion," AIAA 25th Aerospace Sciences Meeting, 12-15 January, Reno, 1987, Paper No. 87-0332.
- [17] Huang, X. Z., "Comprehensive Experiments Studies on Vortex Dynamics over Military Wing Configurations in IAR," 21st AIAA Applied Aerodynamics, 23-26 June, Orlando, 2003, Paper No. 2003-3940.
- [18] Sohn, M. H., and Lee, K. Y., "Experimental Investigation of a Yawed Delta Wing Having Leading Edge Extension," 20th Applied Aerodynamics, 24-26 June, St. Louis, 2002, Paper No. 2002-3267.
- [19] Verhaagen, N. G., Naarding, H. J., 1989, "Experimental and Numerical Investigation of Vortex Flow over a Sideslipping Delta Wing," *Journal of Aircraft*, Vol. 26, No. 11, pp. 971-977.
- [20] Verhaagen, N. G., Jobe, C. E., "Effects of Sideslip on the Characteristics of a 65-deg Delta Wing," 41st AIAA Aerospace Sciences Meeting, 6-9 January, Reno, 2003, Paper No. 2003-0736.
- [21] Worley, J. C., Recktenwald, B. D., "Pyramid Force and Moment Balance Calibration Manual," Auburn University Aerospace Engineering Department, Auburn, AL, 2007 (unpublished).
- [22] Endevco. "Product - 23," URL: <http://www.endevco.com> [cited 13 March 2008].
- [23] US Digital. "Hollow Bore (Hollow Shaft / Thru-bore) Optical Encoder - HB6M," URL: <http://www.usdigital.com/products/hb6m/> [cited 13 March 2008].

APPENDICES

APPENDIX A
ADDITIONAL PLOTS

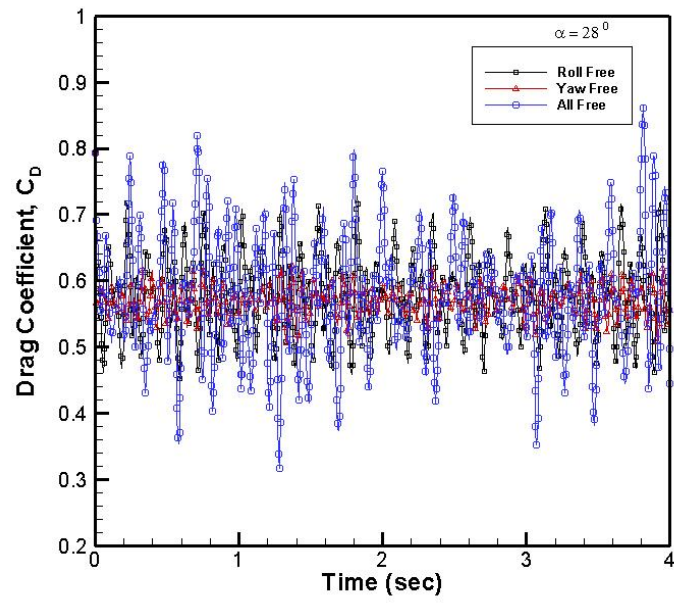


Figure A.1: Drag force coefficient versus time.

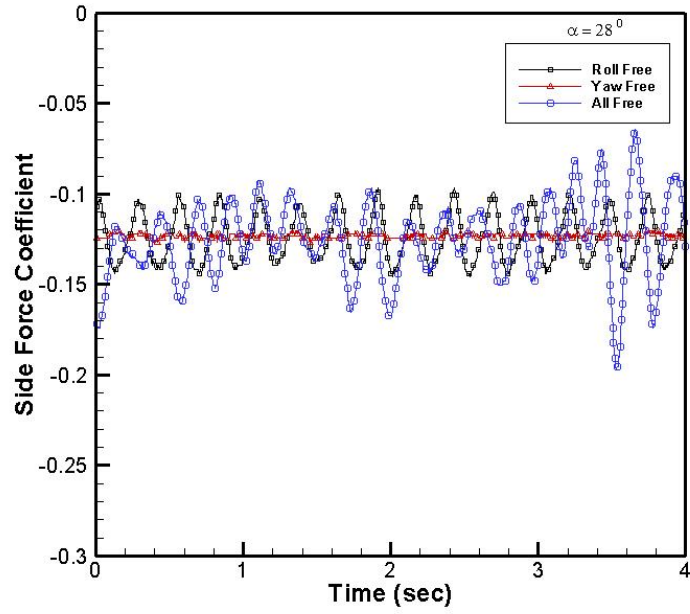


Figure A.2: Side force coefficient versus time.

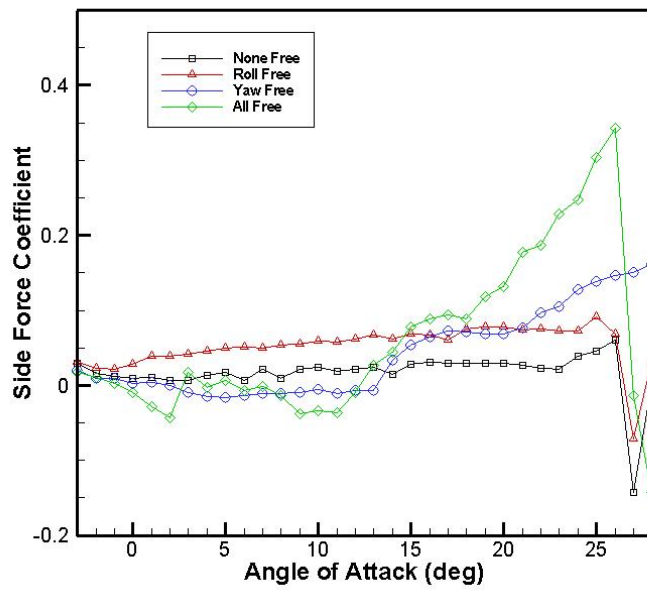


Figure A.3: Side force coefficient versus α .

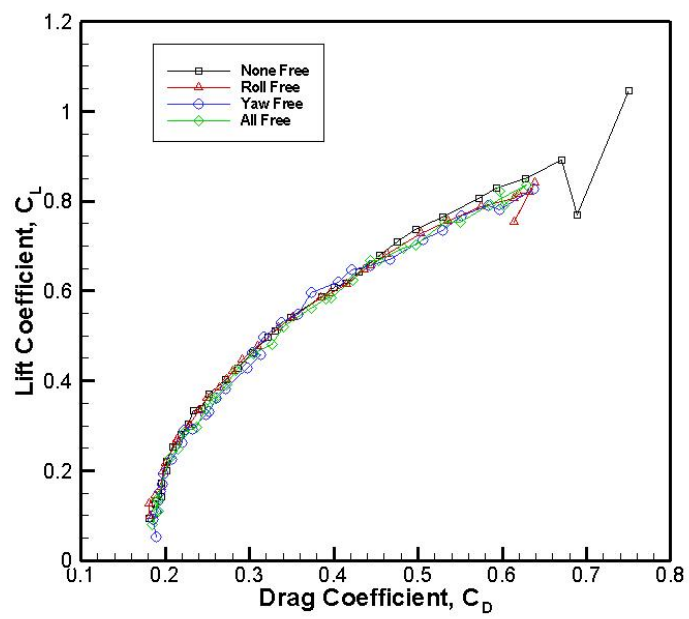


Figure A.4: Lift coefficient versus drag coefficient.